The Astrophysical Journal Supplement Series, 223:1(15pp), 2016 March doi:10.3847/0067-0049/223/1/1

THE *SPITZER*-IRAC/MIPS EXTRAGALACTIC SURVEY (SIMES) IN THE SOUTH ECLIPTIC POLE FIELD

I. Baronchelli[1,2], C. Scarlata[1], G. Rodighiero[2], A. Franceschini[2], P. L. Capak[3], S. Mei[3,4,5], M. Vaccari[6,7], L. Marchetti[8], P. Hibon[9], C. Sedgwick[8], C. Pearson[8,10,11], S. Serjeant[8], K. Menéndez-Delmestre[12], M. Salvato[13], M. Malkan[14], H. I. Teplitz[3], M. Hayes[15], J. Colbert[3], C. Papovich[16], M. Devlin[17], A. Kovacs[1,3], K. S. Scott[18], J. Surace[3], J. D. Kirkpatrick[3], H. Atek[19], T. Urrutia[20], N. Z. Scoville[3], and T. T. Takeuchi[21]
[1] MN Institute for Astrophysics, University of Minnesota, 116 Church Street SE, Minneapolis, MN 55455, USA
[2] Dipartimento di Fisica e Astronomia, Università di Padova, vicolo Osservatorio, 3, I-35122 Padova, Italy
[3] California Institute of Technology, 1200 E. California Boulevard, Pasadena, CA 91125, USA
[4] GEPI, Observatoire de Paris, PSL Research University, CNRS, University of Paris Diderot, 61, Avenue de l'Observatoire F-75014, Paris, France
[5] University of Paris Denis Diderot, University of Paris Sorbonne Cité (PSC), F-75205 Paris Cedex 13, France
[6] Astrophysics Group, Physics Department, University of the Western Cape, Private Bag X17, 7535 Bellville, Cape Town, South Africa
[7] INAF—Istituto di Radioastronomia, via Gobetti 101, I-40129 Bologna, Italy
[8] Department of Physical Sciences, The Open University, Milton Keynes, MK7 6AA, UK
[9] Gemini South Observatory, Casilla 603, La Serena, Chile
[10] RAL Space, Rutherford Appleton Laboratory, Chilton, Didcot, Oxfordshire OX11 0QX, UK
[11] Oxford Astrophysics, Denys Wilkinson Building, University of Oxford, Keble Road, Oxford OX1 3RH, UK
[12] Observatório do Valongo, Universidade Federal de Rio de Janeiro, Rio de Janeiro, Brazil
[13] Max Planck institute for extraterrestrial Physics, Giessenbachstrasse 1, Garching, D-85748, Germany
[14] Department of Physics and Astronomy,UCLA, Physics and Astronomy Building, 3-714, LA CA 90095-1547, USA
[15] Department of Astronomy, Oskar Klein Centre, Stockholm University, AlbaNova University Centre, SE-106 91 Stockholm, Sweden
[16] Department of Physics and Astronomy, Texas A&M University, College Station, TX 77843-4242, USA
[17] Department of Physics and Astronomy, University of Pennsylvania, 209 South 33rd Street, Philadelphia, PA 19104, USA
[18] National Radio Astronomy Observatory, 520 Edgemont Road, Charlottesville, VA 22903, USA
[19] Laboratoire d'Astrophysique, Ecole Polytechnique Fédérale de Lausanne, Observatoire de Sauverny, CH-1290 Versoix, Switzerland
[20] Leibniz Institut für Astrophysik Potsdam, An der Sternwarte 16, D-14482 Potsdam, Germany
[21] Division of Particle and Astrophysical Science, Nagoya University, Furo-cho, Chikusa-ku, Nagoya 464-8602, Japan
Received 2015 September 18; accepted 2016 January 2; published 2016 March 7

ABSTRACT

We present the *Spitzer*-IRAC/MIPS Extragalactic survey (SIMES) in the South Ecliptic Pole field. The large area covered (7.7 deg^2), together with one of the lowest Galactic cirrus emissions in the entire sky and a very extensive coverage by *Spitzer, Herschel, Akari,* and *GALEX*, make the SIMES field ideal for extragalactic studies. The elongated geometry of the SIMES area (≈4:1), allowing for significant cosmic variance reduction, further improves the quality of statistical studies in this field. Here we present the reduction and photometric measurements of the *Spitzer*/IRAC data. The survey reaches depths of 1.93 and 1.75 μJy (1σ) at 3.6 and 4.5 μm, respectively. We discuss the multiwavelength IRAC-based catalog, completed with optical, mid-, and far-IR observations. We detect 341,000 sources with $F_{3.6\mu m} \geqslant 3\sigma$. Of these, 10% have an associated 24 μm counterpart, while 2.7% have an associated SPIRE source. We release the catalog through the NASA/IPAC Infrared Science Archive. Two scientific applications of these IRAC data are presented in this paper. First, we compute integral number counts at 3.6 μm. Second, we use the [3.6]–[4.5] color index to identify galaxy clusters at $z > 1.3$. We select 27 clusters in the full area, a result consistent with previous studies at similar depth.

Key words: catalogs – galaxies: evolution – infrared: galaxies – submillimeter: galaxies – surveys

1. INTRODUCTION

Contrary to the expectation that galaxy formation would proceed via merger-driven bursts of star formation (SF), evidence is now overwhelmingly showing that the bulk of SF in the universe happened in a "quiescent" mode, at increasingly higher average rates at earlier cosmic times (e.g., Daddi et al. 2007; Noeske et al. 2007; Peng et al. 2010; Rodighiero et al. 2011). Although short-lived powerful merger-driven starbursts (SFR $> 1000\,M_\odot\,\mathrm{yr}^{-1}$) do not contribute significantly to the slow process of galaxy growth, they may represent a critical phase in the structural transformation and quenching of the most massive galaxies (e.g., Rodighiero et al. 2011; Bedregal et al. 2013).

The most actively SF galaxies at any redshift also tend to be the most dust-obscured objects. They disappear at rest-frame UV wavelengths and emit most of their energy in the far-IR where they can be easily identified through imaging between 24 and 500 μm. The *Herschel* satellite with its PACS and SPIRE instruments (Griffin et al. 2010; Pilbratt et al. 2010; Poglitsch et al. 2010) have revolutionized the field, producing large samples of mid-IR bright galaxies, selected up to very large redshifts via their bolometric luminosity (e.g., Rodighiero et al. 2010, 2011; Wuyts et al. 2011; Magnelli et al. 2012; Oliver et al. 2012; Rosario et al. 2012; Gruppioni et al. 2013; Santini et al. 2014). To understand the physical nature of these sources, however, detailed sampling of the full spectral energy distribution (SED) and (spectroscopic/photometric) redshifts are needed, and require a secure counterpart association at shorter wavelengths. With secure counterparts and sufficient ancillary data, accurate photometric redshifts can be computed that will allow the effective use of the Atacama Large Millimeter/submillimeter Array, not only to measure spectroscopic redshifts, but also to understand the physical conditions of the molecular gas reservoir in these objects.

In this paper, we present the *Spitzer*-IRAC/MIPS Extragalactic survey (SIMES), an infrared survey carried out with the *Spitzer* Space telescope (Fazio et al. 2004b; Werner et al. 2004) in a 7.7 deg^2 field close to the South Ecliptic Pole (SEP) at 3.6 and 4.5 μm. The SIMES field, centered at (α, δ) = (4^h44^m, $-53°30'$), has Galactic cirrus emission among the lowest in the entire sky (~2–3 MJy str^{-1} at 100 μm, Schlegel et al. 1998; Matsuhara et al. 2006), thus minimizing the extinction in the UV and optical bands as well as maximizing the sensitivity at far-IR wavelengths. This field is therefore very appealing for full multiwavelength exploitation. Furthermore, it has the unique advantage of having an elongated geometry (axial ratio of approximately ~4:1), which minimizes the cosmic variance compared to square fields of similar depth and area on the sky (Trenti & Stiavelli 2008).

The SIMES field has been the target of a vast array of multiwavelength observing programs from major observatories: *Spitzer* (Clements et al. 2011), *Herschel* (Oliver et al. 2012; Wang et al. 2014), *GALEX* (Dale et al. 2007). In particular, together with the North Ecliptic Pole area, it is one of the two fields including the deepest contiguous observations by the *Akari* IR observatory in the context of the *AKARI* Deep Field South survey (Matsuhara et al. 2006; Matsuura et al. 2011). These observations provide us with the most extensive photometric coverage in the mid-IR available for cosmological surveys, of particular relevance for the analysis of dust-obscured active galaxies and AGNs. Very important for the identification at IR and optical wavelengths is the availability of *Spitzer* 24 μm imaging (Rieke et al. 2004), which, with its 5.″0 beam, nicely links imaging at shorter and longer wavelengths. Until our survey, however, the SIMES field was missing the crucial IRAC coverage required to associate the majority of broad-beamed/confused $\geqslant$24 μm sources with physically understood astrophysical objects (detected at $\lambda < 1$ μm). Here we present the new IRAC observations of the SIMES field, targeting this outstanding wavelength gap and thus allowing the full exploitation of the available longer wavelength data. These data will also be crucial for the measurement of physical properties of high-redshift objects, including their photometric redshifts and stellar masses.

The paper is organized as follows. We describe the IRAC observations and catalog preparation in Section 2. The matching with the long wavelength ancillary data is described in Section 3. Finally, we discuss initial results on the 3.6 μm number counts and the identification of intermediate-redshift galaxy clusters in Section 4. Throughout this paper, we assume a standard flat cosmology with $H_0 = 70\,\mathrm{Km\,s^{-1}\,Mpc^{-1}}$, $\Omega_M = 0.3$, and $\Omega_\Lambda = 0.7$. Wherever magnitudes or colors are reported, the AB magnitude system is implicitly assumed.

2. OBSERVATIONS AND DATA ANALYSIS

SIMES is a *Spitzer* Cycle 8 General Observer program (PID 80039, P.I.: Scarlata) observed during the warm mission phase. The SIMES survey in the IRAC bands was designed with the goal of complementing the existing MIPS 24 μm and far-IR observations. The 7.74 deg^2 field was covered in 78 hr with the IRAC instrument in both channels 1 and 2, corresponding to imaging at 3.6 μm and 4.5 μm, respectively. In order to efficiently cover the elongated region, we used multiple 4 × 16 IRAC AORs. This strategy was chosen to minimize the effect of the substantial rotation (1 deg per day) at the field latitude. The field was covered in two visits, between 2011 November 16 and 23, in order to facilitate identification and removal of asteroids. The first and second visits consisted of 3 × 30 s and 2 × 30 s frames, respectively, obtained with a medium cycling dither pattern, for a total exposure time of 150 s. The reduction of the IRAC data generally followed the procedure used by the Spitzer Enhanced Imaging Products (SEIP) mosaic pipeline (Capak et al. 2013) with one additional step. Before the SEIP mosaic processing, a median image was created for each AOR (observing block) and subtracted from the frames to remove residual bias in the frames and persistence from previous observations. The MOPEX Overlap routine (Makovoz et al. 2005) was then used on the background subtracted images to remove any residual background variation from frame to frame. The median subtracted frames were then combined with the MOPEX mosaic pipeline (Makovoz & Khan 2005). The outlier and box-outlier modules were used to reject cosmic rays, transients, and moving objects. Many of the exposures were affected by latent images from prior observations of a bright object, although the impact was much more severe in channel 1 than in channel 2 where it effectively doubled the noise over the background-limited estimate. The effects of these latent images could not be fully mitigated because they faded during the observations, and so a perfect model could not be produced. As a result, the 3.6 μm data have a sensitivity comparable to the 4.5 μm data (see Section 2.2 and Table 2). As a final step, the data were then interpolated onto a 0.″6 pixel scale using a linear interpolation and combined with an exposure time weighted mean combination. Mean, median, coverage, uncertainty, and standard-deviation images were created. The final resulting mosaic is shown in the top panel of Figure 1, while the bottom panel shows a comparison of the IRAC coverage with the coverage in the MIPS, SPIRE, and optical surveys within the same area.

2.1. Source Extraction and Photometry

For the detection and extraction of sources we used the SExtractor software (Bertin & Arnouts 1996) in dual image mode, using the 3.6 μm map as the detection image and the uncertainty map as a weight image. During the detection step, we used a local background calculated over an area of 32 × 32 pixels filtered with a 3 pixel top-hat kernel. We set a 1.5σ threshold, with a minimum of 5 connected pixels above the background noise. For each object we computed AUTO total fluxes, as well as aperture fluxes measured in apertures of 4.″8, 7.″2, and 12.″0 diameter.

SExtractor AUTO fluxes are estimates of the total flux of a source in an elliptical aperture with semimajor axis (a) proportional to the Kron radius of the object (R_K, Kron 1980). We chose $a = 2.5\,R_K$ by setting the SExtractor parameter Kron_fact = 2.5.[22] This choice ensures that the aperture includes more than the 90% of the total galaxy flux[23] (Kron 1980). For apertures with $a < 3.5$ pixels (2.″1), the AUTO flux is computed within a circular aperture. AUTO fluxes account for the real apparent dimension of each source,

[22] In SExtractor nomenclature, a = KRON_RADIUS × A_IMAGE, where A_IMAGE is the luminosity profile rms, in pixels, along the major axis direction, while KRON_RADIUS = Kron_fact × R_K, with R_K in units of A_IMAGE.

[23] The Kron aperture includes a different fraction of the total light of a galaxy, depending on the value of the Sérsic index n of its surface brightness profile (Sérsic 1963; Graham & Driver 2005).

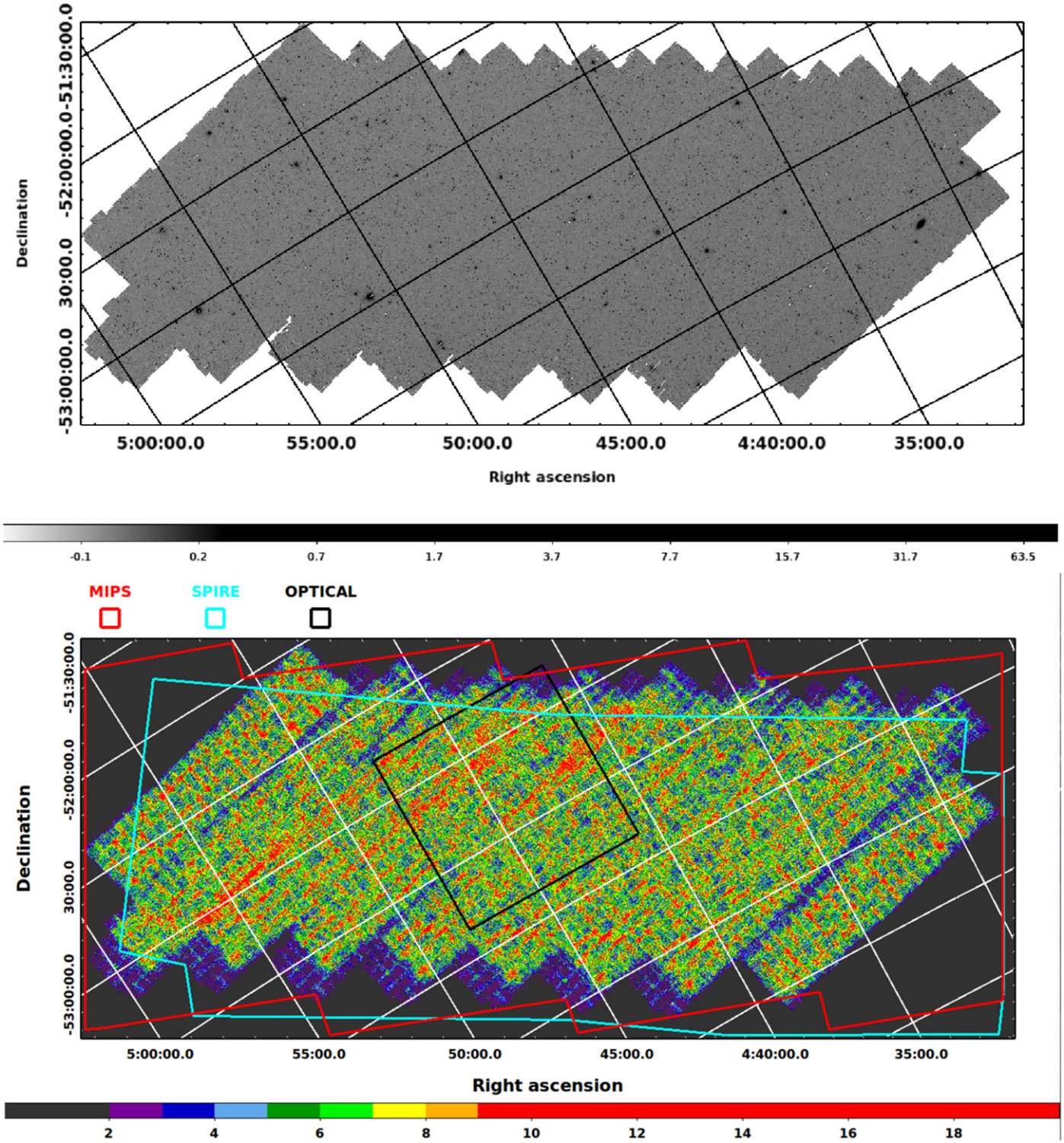

Figure 1. Top panel: IRAC 3.6 μm mosaic of the SIMES field. The color scale is in units of MJy sr^{-1}. Bottom panel: Coverage map at 3.6 μm. The color scale shows the number of frames per pixel. The areas covered by MIPS, SPIRE, and WFI-R_c (optical) are shown in red, cyan, and black, respectively.

the elliptical shape of the observed isophotes and the source's radial surface brightness profile.

In Figure 2, we report the mean ratio $\langle R \rangle$ between the AUTO fluxes and the APERTURE fluxes computed for our sources in bins of semimajor axis. $\langle R \rangle$ increases with the increasing apparent dimension of the sources, indicating that a fraction of the sources' emission is missed when using a fixed aperture. There is a strong linear correlation between $\log \langle R \rangle$ and the semimajor axis of the elliptical aperture, with different slopes depending on the size of the circular aperture used. The ratio becomes $\sim$1 when the semimajor axis of the elliptical aperture has a dimension similar to that of the circular aperture used for the comparison. When considering the smallest elliptical apertures and the largest circular apertures, we observe a large

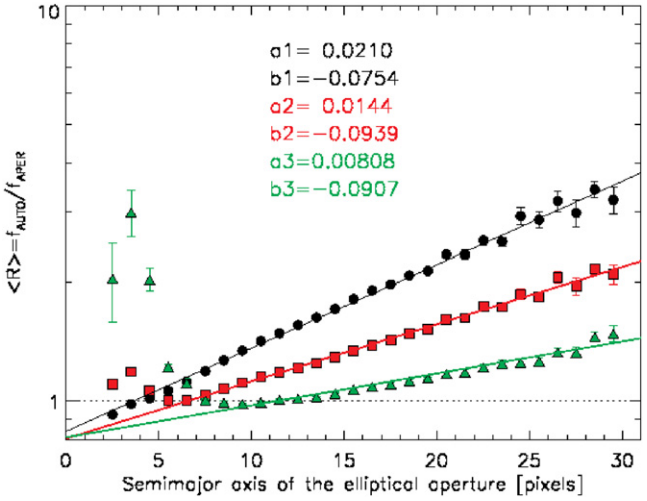

Figure 2. Average ratio between AUTO fluxes and uncorrected aperture fluxes (4.″8 in black, 7.″2 in red, 12.″0 in green), as a function of the semimajor axis of the Kron elliptical aperture, together with best linear fit coefficients, expressed as $\log\langle R\rangle = a \times$ (semimajor axis) $+ b$. The figure shows how an increasing amount of the source's emission is missed when using fixed circular apertures to compute fluxes.

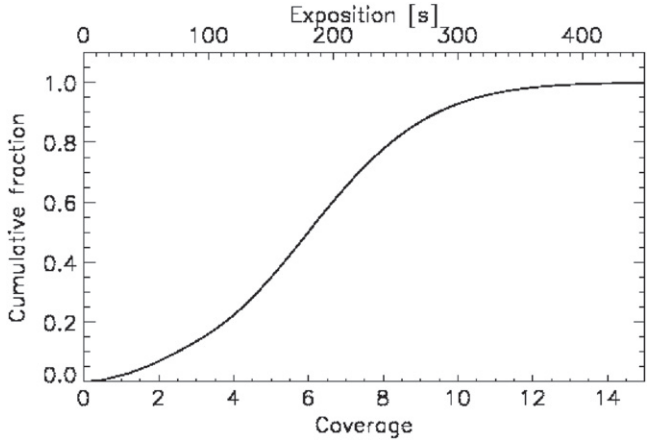

Figure 3. Cumulative distribution of the pixel coverage. More than 70% of the pixels in the mosaic are at the nominal 150 s coverage.

deviation from $\langle R\rangle \sim 1$. This effect is likely due to an overestimate of the background that becomes appreciable when the elliptical and circular apertures have very different sizes. Sources characterized by small apparent dimensions (i.e., small semimajor axis of the elliptical aperture) tend to have smaller aperture fluxes for larger aperture sizes (green curves in Figure 2). Thus, hereafter, all fluxes reported are total fluxes "FLUX_AUTO" measured within the Kron SExtractor apertures.

2.2. Survey Sensitivity

The mapping strategy adopted to cover the large SIMES area results in varying coverage across the field with a resulting noise variation. Figure 3 shows the cumulative distribution of the pixel coverage in the 3.6 μm mosaic, where the coverage on the horizontal axis is defined as the number of 30 s exposures per pixel. More than 70% of the mosaic is at or above the planned coverage of 150 s.

In order to identify reliable detections in the 3.6 μm catalog, we follow Surace et al. (2005) and compute a coverage-based signal-to-noise ratio (S/N) for each source. Surace et al. (2005) compute the noise σ corresponding to the mean coverage within the mosaic ($\langle C\rangle$, where C is the number of exposures per pixel) and then scale it by a factor f that accounts for the specific coverage, C, of the aperture used for the flux measurement, i.e., $f = \sqrt{\langle C\rangle/C}$. This procedure assumes that the noise scales as the square root of the exposure time. However, the noise contribution from faint unresolved sources could be substantial in the deepest regions of the mosaic.

In order to check the $t_{\rm exp}^{-0.5}$ assumption, we empirically derived the noise properties of the mosaic as a function of the actual coverage. First, we measured the flux in 8 pixel diameter apertures distributed in a homogeneous grid covering the mosaic. Then, we divided our measures in different groups, according to the coverage underlying the apertures in which they were obtained. In each bin of coverage, we fitted a Gaussian function to the distribution of aperture fluxes, symmetrized with respect to the median to include only background-dominated apertures. The standard deviation of the best-fit Gaussian distribution in each bin of coverage is then a measurement of the average background noise corresponding to that coverage.

To check the normal distribution of the pixels noise, we applied both the Kolmogorov–Smirnov (K–S) and Anderson–Darling (A–D) tests to the negative side of the pixel flux distribution. Because the noise level is expected to depend on the exposure time, we consider seven equally sized bins of coverage ranging between 2 and 10. At the nominal coverage of 5, using the K–S test, the probability of finding the computed difference $D = 3.9 \times 10^{-3}$ between the cumulative distribution of fluxes and that expected from a normal distribution is 0.74. Using the A–D test, we found a difference of $A^2 = 0.55$, which is close to the reference value of 0.576, corresponding to the rejection of the null hypothesis (normality) with a 15% level of significance. At lower and higher coverages, the probability from the K–S test ranges from 0.28 to 0.96, while A^2 ranges from 0.49 to 1.87, indicating that when a deviation from the normal distribution is present, it is small.

In Figure 4, we show the resulting σ as a function of average coverage $\langle C\rangle$ in each of the six bins. The dependency with C is in agreement with the Poissonian approximation (shown with a continuous red line). The theoretical curve is normalized at the nominal coverage of the survey ($C = 5$). The trend between σ and C is well reproduced by the relation $\sigma \propto C^{-\alpha}$, with $\alpha = 0.43 \pm 0.09$ (green dashed line in Figure 4). To calculate the S/Ns, we computed APERTURE flux and noise in the same aperture (4.″8 diameter). For each source, the underlying coverage is computed as the median value in the aperture. We retain in the final catalog only sources with 3.6 μm flux above 3σ. The final IRAC-based catalog constructed in this way includes 341,006 sources.

We compute the sensitivity of the 4.5 μm observations using the same method described for the 3.6 μm data. Again, measuring σ as a function of the average coverage, we found an agreement with the Poissonian expectation, with α (4.5 μm) $= 0.53 \pm 0.08$.

At all coverages, we found a 4.5 μm depth σ comparable to or smaller than that measured at 3.6 μm. In particular, at the nominal coverage of the survey, we measure $\sigma = 1.93$ μJy at 3.6 μm and $\sigma(C = 5) = 1.75$ μJy at 4.5 μm. As noted before,

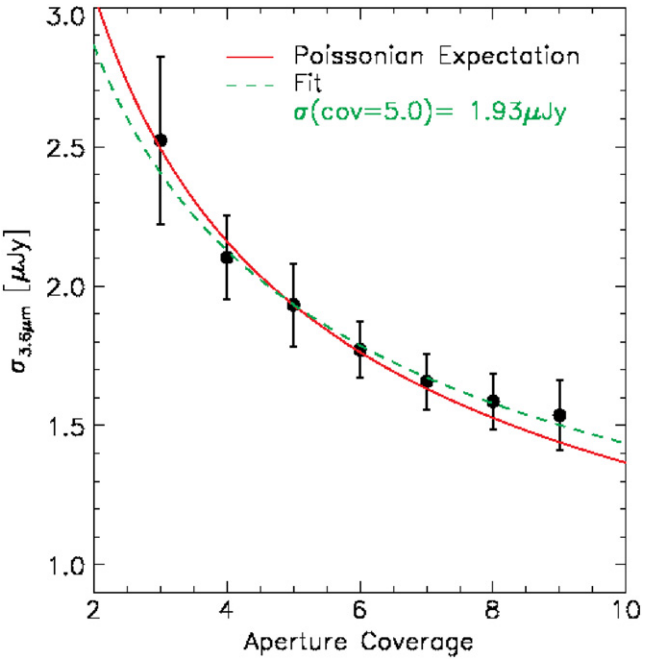

Figure 4. Sky background noise, σ, as a function of aperture coverage (see the text for details). The expected trend for background-dominated noise is shown with a red solid line, while the observed best-fit relation is shown with a green dashed line. We cut the IRAC 3.6 μm catalog at a 3σ level, where σ is estimated from the average coverage of each source.

this behavior is due to the effect of latent images being more pronounced in the 3.6 μm channel than in the 4.5 μm channel.

2.3. Survey Completeness and Contamination

We estimated the survey completeness as a function of the 3.6 μm flux, adding artificial sources to the original IRAC mosaic and extracting them with the same procedure used for the real IRAC map. To create the artificial sources, we generated a synthetic point-spread function (PSF) using the median of 76 images of point sources extracted from the original 3.6 μm map. These sources were selected for being isolated (closest counterpart distance $>22\farcs0$) and with fluxes near 100 μJy. Moreover, we excluded clearly extended sources, characterized by KRON_RADIUS $\times$ A_IMAGE $>$ 10 pixels and sources located at the edge of the map.

We simulated approximately 69,000 artificial sources with 31 different 3.6 μm fluxes in the range ~3–100 μJy. For each of the 31 groups, we simulated an independent IRAC map, randomly distributing 2233 same-flux artificial sources along with the real ones. After the extraction, we computed the detection rate (i.e., the completeness) as the ratio between the number of sources inserted in the map and the recovered ones. This approach allows us to maximize the number of sources inserted in the maps without artificially increasing the spatial density of the sources, as would happen if we added all the simulated sources at once. The results of this analysis are presented in Figure 5, where we show that the completeness drops below 50% at 3.6 μm flux of approximately 9.0 μJy (corresponding to a source flux of approximately 4.7σ).

We also investigate the flux accuracy as a function of the artificial source flux by computing the average difference between the flux of the simulated sources and their flux after the extraction. The results, presented in the bottom panel of

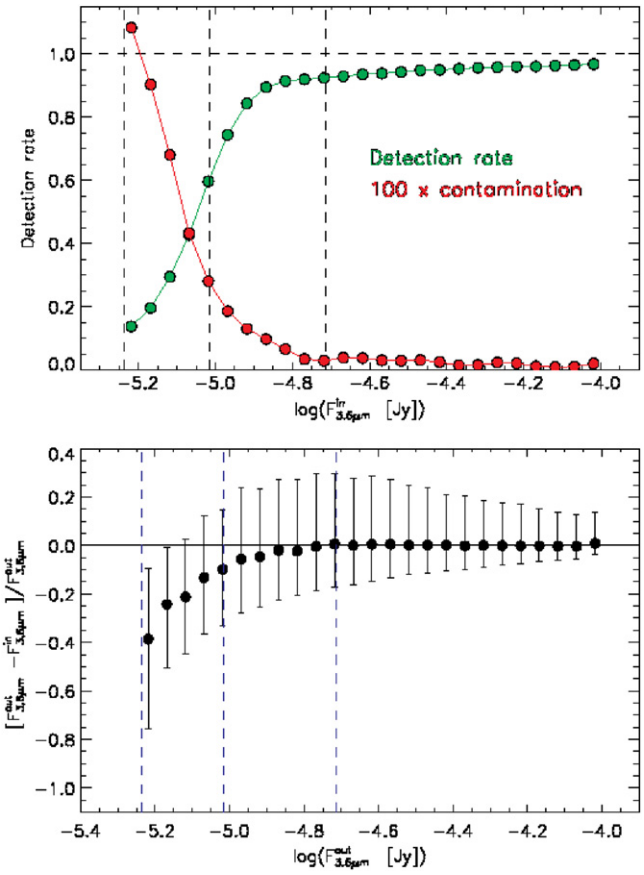

Figure 5. Top panel: completeness and contamination computed through numerical simulations. The completeness level drops to approximately 50% at 3.6 μm flux ~9 μJy. The contamination rate (multiplied by a factor of 100, for clarity) reaches a maximum of 1.1% at the 3σ flux. Bottom panel: Flux accuracy of the simulated sources. The error bars represent the 1σ range of flux accuracy resulting from the simulations. Source fluxes start to become systematically underestimated (by more than 10%) below ~9 μJy. The vertical dashed lines show our 3, 5, and 10σ flux limits.

Table 1
Completeness as a Function of 3.6 μm Flux

Completeness (%)	Flux 3.6 μm (μJy)
50	9.0
75	10.8
90	14.1
95	40.0
97	107.1
99	224.2

Figure 5, show that the accuracy of the flux measurements is a function of the output fluxes. For sources at a 3σ level, the recovered flux ranges (1σ of the data distribution) from ~75% to ~10% below the input flux, while for sources at the 10σ level the range is from ~20% below to ~30% above the input flux. There is an indication that faint sources ($F_{3.6\mu m} < 5\sigma$) have systematically underestimated fluxes, although the scatter in this range is also larger. The detection rate as a function of the 3.6 μm flux is summarized in Table 1. These values have been used for computing the 3.6 μm number counts presented in Section 4.1.

Table 2
Available Ancillary Data

Band (μm)	Instrument	Overlap Area[a] (deg^2)	Depth	Number of Identified Counterparts[b]			
				All	MIPS 24	SPIRE	MIPS 24 and SPIRE
3.6	IRAC	7.74	5.80 μJy (3σ)[c,d]	341006	25132	9447	7041
4.5	IRAC	7.26	5.25 μJy (3σ)[d]	320460	23688	9320	6947
24	MIPS	7.66	0.26 mJy (50% compl.)[e]	25132 (60)	25132 (60)	7041 (60)	7041 (60)
70	MIPS	7.66	24 mJy (50% compl.)[e]	882	882	692	692
250	SPIRE	6.52	15.6 mJy (3σ)[f]	8743 (50)	6666 (50)	8743 (50)	6666 (50)
350	SPIRE	6.52	12.7 mJy (3σ)[f]	9416 (60)	7015 (60)	9416 (60)	7015 (60)
500	SPIRE	6.52	18.5 mJy (3σ)[f]	8624 (58)	6354 (58)	8624 (58)	6354 (58)
0.65	WFI	1.13	0.53 μJy (3σ)	27585	2279	808	680

Notes.
[a] Area covered in both the IRAC 3.6 μm band and in the band indicated in the first column.
[b] The additional number of MIPS–SPIRE sources without 3.6 μm counterparts is indicated in parenthesis.
[c] The IRAC 3.6 μm catalog is cut at a 3σ level, as described in the text, keeping into account the underlying coverage for each source. Sources with fluxes below the value reported in the table can consequently be found in the catalog.
[d] The value of σ reported is estimated for the nominal coverage of the survey ($C = 5$).
[e] From Clements et al. (2011). Minimum 24 μm flux in the catalog: 0.20 mJy. Minimum for MIPS identified sources with a SPIRE counterpart: 0.31 mJy.
[f] 1σ values from Oliver et al. (2012). We included in our catalog only the sources with a flux higher then 3σ in at least one of the SPIRE bands.

We estimate the false positive rate (i.e., contamination rate) applying the same extraction technique and 3σ cut used for the original 3.6 μm map, to the inverted 3.6 μm image (pixel fluxes multiplied by -1). We obtain a total contamination rate of 0.21%. In Figure 5, the contamination (multiplied for a factor of 100) is shown as a function of the flux of the spurious extracted sources. Spurious sources represent ~1.1% of all sources at the 3σ level and ~0.25% at 5σ. In order to obtain an independent upper limit to the total contamination rate, we apply the B–H test (Benjamini & Hochberg 1995) under the assumption that the background distribution is known and Gaussian. For each flux in the catalog we can then compute its p-value under the null hypothesis that it was extracted from the background population. The p-value relative to the 3σ flux threshold adopted for the 3.6 μm catalog ($p_{3\sigma}$) corresponds to the value $C(p_{3\sigma})$ in the p-values cumulative distribution. The expected contamination rate $\epsilon = (1 - \alpha)\, Np_{3\sigma}/C(p_{3\sigma}) < Np_{3\sigma}/C(p_{3\sigma})$, where N is the number of apertures used in the test and α is the ratio between the number of spurious and real sources in the catalog. At the nominal coverage of 5, the upper limit on the contamination rate is then 1.2%.

3. ANCILLARY DATA

The SIMES field is fully covered with both *Spitzer* MIPS (24 and 70 μm), and *Herschel* SPIRE (250, 350, and 500 μm) as well as by *Akari*. In the present paper we report on the MIPS and SPIRE observations, while the *Akari* data will be discussed in a forthcoming paper (I. Baronchelli et al. 2016, in preparation). The central square degree is also covered by optical imaging (see Figure 1). In the following sections we describe how we merged the IRAC-based catalog with the publicly available MIPS (Clements et al. 2011) and SPIRE (*HerMES*, DR2, Roseboom et al. 2010; Oliver et al. 2012; Smith et al. 2012; Wang et al. 2014) catalogs. Section 3.3 describes the data reduction, photometry, and matching of the optical data. The main properties of the multiwavelength data are summarized in Table 2.

3.1. MIPS 24 and 70 μm

The MIPS 24 μm catalog is described in Clements et al. (2011). The Clements et al. (2011) catalog covers an area of ~12 deg^2 in the SEP region and includes counterparts at 70 μm of the 24 μm detected sources, and so we limit the analysis to the cross-correlation between IRAC and MIPS 24 and report the 70 μm association identified in the original MIPS catalog. Clements et al. (2011) estimate that the 24 μm catalog is 50% complete at 0.26 mJy and 80% complete at 0.32 mJy, while the source reliability is 96% at 0.285 mJy.

In order to identify the most likely IRAC counterpart to each MIPS source, we proceed as follows. For each MIPS 24 μm source, we searched the IRAC catalog for the nearest object inside a radius equal to the quadratic sum of the σ of the PSF of the two instruments (i.e., a search radius of $2\farcs6$). In the matching process, we identified a small systematic shift[24] (of the order of ΔR.A. $= 0\farcs099$, Δdecl. $= 0\farcs49$) between the two catalogs. Therefore, we corrected the MIPS positions before searching for the nearest IRAC counterpart. We report in the final catalog both the corrected and the original coordinates of the sources in each band. In Table 3, we report the distance and the average R.A. and decl. shifts of all of the sources matched in the catalog. When multiple IRAC sources were found within the search area (see Figure 7), we associated the closest IRAC object. This happens for 514 MIPS sources which we flag as uncertain identifications ("N_IRAC_MIPS" parameter greater than one). All the other potential IRAC counterparts can be found in the catalog. Of all of the MIPS sources (25,132 objects), 98.0% have a unique IRAC counterpart within a region of $2\farcs6$ radius. MIPS sources without an IRAC counterpart are generally not included in our catalog. The only exception is represented by 60 visually checked sources in the IRAC covered area with a reliable SPIRE counterpart.

3.2. SPIRE 250, 350, 500 μm

The SIMES field was observed as part of the *Herschel* Multi-tiered Extragalactic Survey (HerMES, Oliver et al. 2012; Wang et al. 2014). The second data release of the SPIRE XID catalogs (DR2, Roseboom et al. 2010; Smith et al. 2012; Wang et al. 2014) covers approximately 84% of the field, and

[24] We verified that the shift did not depend on the position in the large mosaic, thus indicating that any distortion in the IRAC mosaic was properly accounted for.

Table 3
Parameters Used in the Counterpart Identification Procedure[a]

Band	Search Radius (″)	Mean Distance[b]		Barycentre Position (ΔR.A., Δdecl.)[c]		ΔN
		Before R. (″)	After R. (″)	Before R. (″)	After R. (″)	
MIPS	2.60	1.01	0.87	0.098, 0.49	0.010, 0.071	+140 (0.6%)
SPIRE[d]	8.04	3.00	3.00	0.019, −0.045	0.0035, −0.0040	−1 (0.01%)
2MASS	2.68	0.60	0.59	0.067, −0.067	0.0061, −0.0059	+7 (0.005%)

Notes.
[a] All the values are computed before the correction for average shift (Before R.) and after the correction (After R.).
[b] Average distance, in arcseconds, between the IRAC 3.6 μm sources and the corresponding counterparts in the other bands.
[c] Average difference (ΔR.A., Δdecl.) between the IRAC 3.6 μm sources and the corresponding counterparts in the other bands.
[d] Distances refer to the MIPS 24 positions.

includes all sources identified at the 1σ level at 250, 350, or 500 μm. Here, we keep only those sources with fluxes above 3σ in at least one SPIRE band.

The large size of the SPIRE PSF (18.″0 at 250 μm) prevents us from directly cross-correlating the SPIRE and IRAC catalogs. Instead, we exploited the MIPS 24 μm detections as a "bridge" between the two wavelengths, i.e., we searched the SPIRE counterparts given the MIPS 24 prior position. We performed a direct SPIRE–IRAC correlation only when a SPIRE source did not have a MIPS counterpart. As we did for the MIPS–IRAC correlation, before correlating the SPIRE and MIPS counterparts, we corrected the SPIRE coordinates for the small average offset between MIPS and SPIRE positions using the original MIPS coordinates as reference. In our catalog, we report both the original SPIRE (R.A., decl.) coordinates as well as the coordinates corrected to the average SPIRE–MIPS and then MIPS–IRAC shifts.

Given the MIPS positions, we searched the SPIRE counterparts inside a radius of 8.″04 (quadratic sum of the PSF's σ of the two instruments). When a single SPIRE source is associated with two (or more) different MIPS sources, we consider both associations. Both the SPIRE and MIPS fluxes are proportional to the total IR luminosity ($L_{\rm IR}$, e.g., Chary & Elbaz 2001; Elbaz et al. 2011). This is due to the same thermal origin of the radiation emitted in these bands. Given this assumption, when we find multiple MIPS counterparts for a single SPIRE source, the original fluxes in the three SPIRE bands are divided among the MIPS counterparts proportionally to their 24 μm flux. This multiple association involves 429 MIPS sources, flagged in our catalog through a N_MIPS_SPIRE parameter greater than 1. SPIRE–MIPS associations outside the IRAC covered area are not included in our catalog. Using the MIPS 24 prior position, we found 7034 SPIRE counterparts for our IRAC sources.

For the remaining SPIRE sources without a MIPS counterpart, we searched for a direct IRAC–SPIRE association. We found 2413 SPIRE sources with associated IRAC counterparts. These are flagged in the catalog with N_IRAC_SPIRE $>$ 0 and N_MIPS_SPIRE $\leqslant$ 0. The MIPS-undetected SPIRE sources have 24 μm flux below the detection threshold in this band. This is because for SPIRE detected sources, the detection rate at 24 μm strongly depends on the source redshift. This is due to the typical shape of the SED of far-IR detected sources[25], usually presenting a bump of emission centered at $\lambda_{\rm R.F.}^{\rm dust} \sim 100$ μm (Kirkpatrick et al. 2012). This bump is due to the thermal emission of dust

[25] Some examples of typical SEDs for different types of galaxies can be found in, e.g., Polletta et al. (2007).

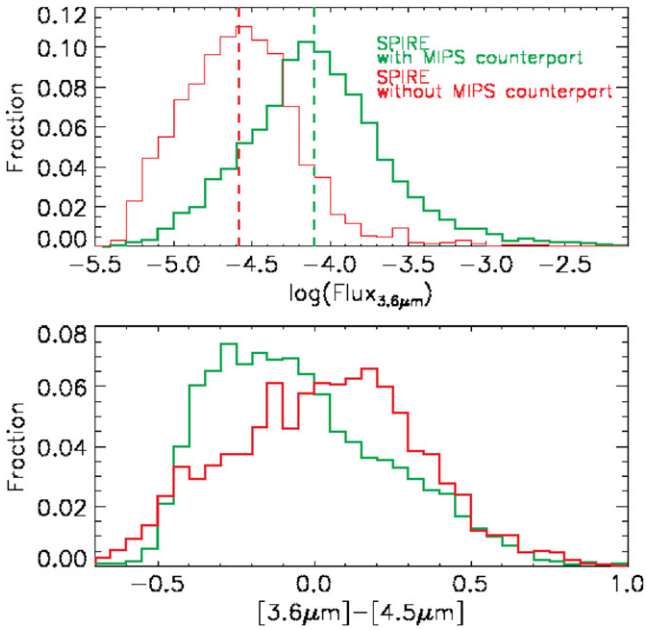

Figure 6. MIPS-undetected SPIRE sources are likely located at higher redshift than MIPS-detected sources. Normalized 3.6 μm fluxes (top panel) and [3.6 μm]–[4.5 μm] AB color distributions (bottom panel) for SPIRE sources in our catalog. The SPIRE sources with and without MIPS counterparts are indicated in green and red, respectively. The median of each distribution is represented with a dashed line in the same color code.

heated by optical-UV radiation produced by young stars inside star forming regions or by accretion disks of active galactic nuclei (AGNs). At increasing redshifts, the SPIRE bands sample spectral regions closer to the redshifted peak. Instead, being located on the opposite side of the thermal emission bump, the MIPS 24 μm band samples a spectral region whose the emitted luminosity tends to be lower at higher redshifts. The combination of these effects is responsible for the lower MIPS detection rate among the SPIRE detected sources at higher redshifts. This is demonstrated in Figure 6 where we show the distributions of 3.6μm flux and [3.6 μm]–[4.5 μm] colors (i.e., $2.5\log(F_{4.5\ \mu{\rm m}}/F_{3.6\ \mu{\rm m}})$) for SPIRE sources with and without MIPS counterpart. The two IRAC bands sample the stellar 1.6 μm bump (Simpson & Eisenhardt 1999; Sawicki 2002) and the IRAC color is expected to change with redshift as the peak moves through the two filters. The color distributions in Figure 6 are clearly different, indicating that MIPS-undetected SPIRE sources are more commonly located at higher redshifts than the MIPS-detected SPIRE sources. This is

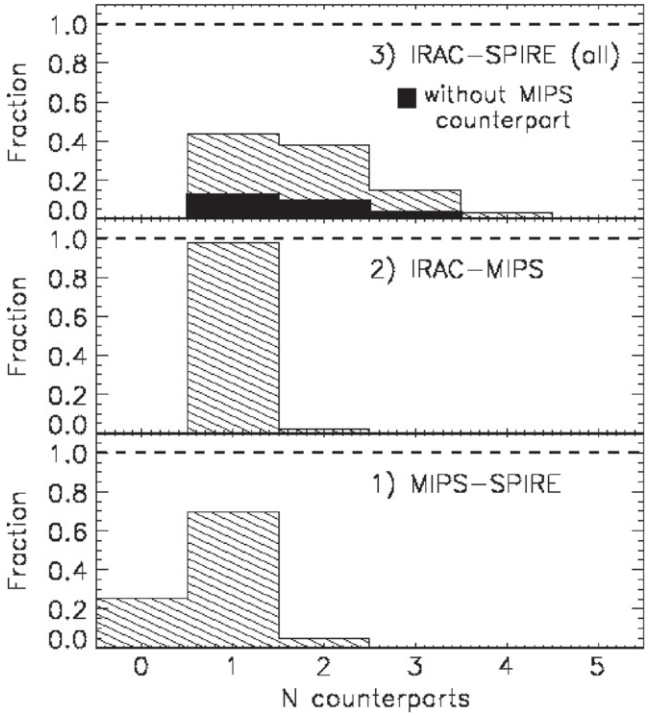

Figure 7. Fraction of sources with one or multiple counterparts inside the search radius for the SPIRE–MIPS, MIPS–IRAC, and SPIRE–IRAC positional correlations. In the top panel, we show the distribution of the number of IRAC counterparts inside the SPIRE–IRAC search aperture for the full sample of SPIRE sources (hatched histogram). The black filled histogram shows the distribution of the number of IRAC counterparts for SPIRE sources without a MIPS counterpart.

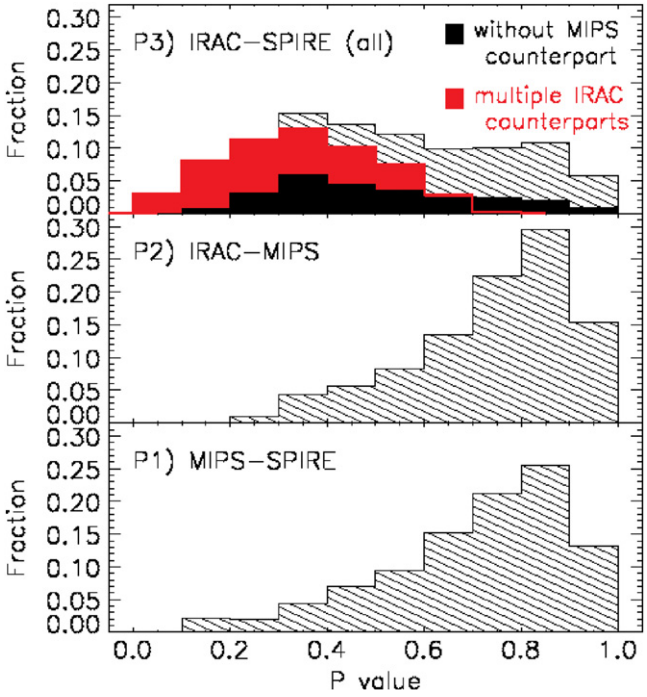

Figure 8. Correlation reliability indicator—*P*—computed for the SPIRE–MIPS (*P*1), MIPS–IRAC (*P*2), and SPIRE–IRAC (*P*3) positional correlations. The latter was computed for all SPIRE sources in our catalog, even when the correlation with IRAC is found through the MIPS position. The black filled distribution in the top panel shows SPIRE sources without a MIPS counterpart. The red filled distribution is computed for SPIRE sources with multiple IRAC counterparts inside the IRAC–SPIRE search radius.

also supported by the lower median 3.6 μm flux of the MIPS-undetected SPIRE sources (upper panel of Figure 6).

SPIRE sources lacking an IRAC counterpart are generally not included in our catalog. However, we include in our catalog the 60 SPIRE sources with a reliable MIPS counterpart but without any IRAC counterpart inside a distance corresponding to two times the IRAC–MIPS search radius. We visually checked all of the sources in the IRAC 3.6 μm image in order to exclude missed detections due to the presence of nearby bright sources or border effects enhancing the noise, and consequently, the detection threshold.

The catalog includes a total of 9447 SPIRE sources with a SPIRE flux (in at least one band) above 3σ. The reliability of their association with the IRAC counterpart is discussed in the next section.

3.2.1. Counterpart Reliability

The probability of having the right MIPS (IRAC) counterpart associated with the SPIRE (MIPS) source depends on both the number of galaxies found within the search area, as well as the distance to the identified counterpart(s). In Figure 7 we show the fraction of MIPS and SPIRE sources with one or more IRAC or MIPS counterpart inside the search radius. Only ∼2% of our MIPS sources have more than one single IRAC counterpart inside the search radius. In all these cases we consider the closest IRAC source as the only real counterpart. Instead, ∼6% of our SPIRE–MIPS associations are made dividing the SPIRE fluxes among the multiple MIPS counterparts, as explained in Section 3.2. In the direct SPIRE–IRAC associations we considered the closest IRAC sources as the only real counterparts, but in this case, only ∼48% of our SPIRE source have a single IRAC counterpart inside the searhing radius. In order to assess the reliability of the matched counterparts, we develop a parameter, *P*, that accounts for both the counterpart distance and the number of sources found in the search radii.

As mentioned earlier, we define the search area by the radius r_s equal to the the quadratic sum of the PSF's σ of the two instruments involved (e.g., $r_s = \sqrt{\sigma^2_{\rm IRAC} + \sigma^2_{\rm MIPS}}$, for IRAC–MIPS correlation). We consider a normalized 2D Gaussian function with $\sigma = r_s$; the counterpart distance d_i is always smaller then r_s. We then compute the quantity A_i as the probability of the galaxy being at a distance greater than d_i, for the given Gaussian function. For a single counterpart, centered on the coordinates of the starting objects, $A_i = 1$; in general, A_i decreases as the distance of the counterpart increases. We then account for the presence of multiple counterparts (at different d_i), by defining the parameter *P* as follows:

$$P = A_1 \frac{A_1}{\sum_i A_i}, \quad (1)$$

where A_1 is defined as A_i corresponding to the closest counterpart. For multiple counterparts the factor $A_1/\sum A_i$ is smaller than one, and decreases with the number of counterparts.

We computed the values of *P* for the SPIRE–MIPS (*P*1), MIPS–IRAC (*P*2), and SPIRE–IRAC (*P*3) correlations. The distributions of the *P* values are represented in Figure 8. The direct SPIRE–IRAC correlation is studied for the whole SPIRE

sample in our catalog, considering also the sources for which we found a correlation through the MIPS position.

The MIPS–IRAC and SPIRE–MIPS association reliability is usually high, as demonstrated by the distribution of $P1$ and $P2$. As a consequence, the association of the SPIRE sources with the IRAC counterparts through the MIPS position is still reliable, even if the $P3$ distribution is not as narrow as those of $P1$ and $P2$.

Using a Monte Carlo simulation, we assessed the reliability of those associations in which multiple MIPS counterparts are associated with individual SPIRE sources (see Section 3.2). The same simulation also allows us to determine the reliability of the direct SPIRE–IRAC associations. The simulation is performed by first randomly shifting the position of the SPIRE sources to 10, 20, 30, and 50 times the search radius from the original position and then looking for potential IRAC counterparts. We found a detection rate of approximately 49.7% $\pm$ 0.1%.

In our catalog, among the SPIRE counterparts found through a MIPS prior position, the fraction of SPIRE sources having multiple IRAC potential associations is 57.6%. SPIRE sources with MIPS counterparts are generally associated with high flux IRAC counterparts: only 4.0% of them have an IRAC flux below the 90% completeness limit (see Table 1). Moreover, multiple IRAC counterparts in a MIPS–IRAC search radius are very rare. This means that purely geometrical MIPS–IRAC associations are highly improbable. Therefore, we can safely assume that for almost all our SPIRE counterparts found through MIPS prior positions, there is a detected IRAC real counterpart. Given these assumptions and the results of our simulation, we expect that 49.7% of the SPIRE sources, aside from the real IRAC counterpart, have an additional purely geometrical association. Since we measure a real multiple association rate of 57.6%, the additional 7.9% of these SPIRE sources must have real multiple IRAC components. Indeed, in our catalog, ~6.1% of the SPIRE sample have multiple MIPS counterparts, and all of them have one IRAC counterpart inside the MIPS–IRAC search radius. The ~2% difference confirms the reliability of the multiple SPIRE–MIPS associations discussed in Section 3.2.

As can be observed in the top panel of Figure 6, the 3.6 μm flux for the SPIRE sources is generally lower when they are not detected at 24 μm. As explained in Section 3.2, the lower IRAC flux of these MIPS-undetected sources can be explained with the higher median redshift of the these sources. We find that ~24% of this sample are below the 90% completeness level, resulting in an overall completeness of ~85%. Therefore, the probability of detecting the real counterpart inside the search radius is $P_{\rm det}^{\rm real} = 0.85$ while, from our simulation, the probability to find a purely geometrical IRAC counterpart is $P_{\rm det}^{\rm geom} = 0.497$. We define the following products:

$$P_1 = P_{\rm det}^{\rm geom}(1 - P_{\rm det}^{\rm real}), \quad (2)$$

$$P_2 = P_{\rm det}^{\rm geom} P_{\rm det}^{\rm real}, \quad (3)$$

$$P_3 = (1 - P_{\rm det}^{\rm geom})(1 - P_{\rm det}^{\rm real}), \quad (4)$$

$$P_4 = (1 - P_{\rm det}^{\rm geom}) P_{\rm det}^{\rm real}. \quad (5)$$

Each SPIRE source can either have a possible counterpart (with probability $P_{\rm det} = P_1 + P_2 + P_4$) or not ($P_{\rm no\text{-}det} = P_3$), with $P_1 + P_2 + P_3 + P_4 = 1$. All SPIRE sources in our catalog have one IRAC association. Assuming that the SPIRE position is always closer to the real IRAC counterpart than to the nearest geometrical association, their reliability can be estimated as:

$$P_{\rm det}^{\rm real}({\rm cat}) = \frac{P_2 + P_4}{P_1 + P_2 + P_4} \sim 0.92. \quad (6)$$

In reality, if a purely geometrical IRAC counterpart is present, it can be closer to the SPIRE position than the real counterpart. This is more probable when the IRAC–SPIRE distance is higher (and consequently the $P3$ parameter lower). Moreover, as stated before, about 6%–8% of the SPIRE sources have more than a single real counterpart, further reducing the reliability for this sample. For all SPIRE sources in our catalog we report the number of potential IRAC counterparts in the search radius (N_IRAC_SPIRE) and the parameter $P3$.

3.3. Optical R_c Band

A central area of approximately one square degree was observed at the MPG/ESO 2.2 m telescope at La Silla with the Wide Field Imager (WFI) during 2010 October (P.I.: T. Takeuchi). The eight CCDs of the WFI camera cover a total area on the sky of $34' \times 33'$, with a pixel scale of $0\farcs24$. Four pointings with the R_c broadband filter ($\lambda_c = 6517.25$ Å) were obtained, covering a total area of 1.13 deg^2. Each pointing was observed with multiple exposures dithered to optimally remove the gaps between different CCDs and other CCD defects. The total exposure time varied between 2.2 and 1 hr.

The data were reduced with standard IRAF routines included in the NOAO mosaic software MSCRED. A Super-sky Flat-field correction was applied by dividing all of the science frames for the average of the non-aligned and source-subtracted science exposures. The final R_c mosaic was created combining the images on the four pointings. In the final mosaic, the FWHM of the PSF was $1\farcs0$.

Sources were extracted from the final mosaic using the SExtractor software. We considered only sources with five connected pixels above a threshold of 1.0σ of the local background For each detected object, we recorded in the catalog the total AUTO flux. The photometric calibration of these data is obtained through the comparison with Bruzual & Charlot (2003, BC03) template SEDs fitted to a large set of optical data. We used a set of measures obtained in the SIMES field for a selected sample of sources, in 13 different filters covering the spectral range between the u and the IRAC 4.5 μm bands (I. Baronchelli et al. 2016, in preparation). Knowing the spectroscopic redshift of the selected sources (Sedgwick et al. 2011), we used a χ^2 minimization technique (i.e., hyperzmass, Bolzonella et al. 2000) to find the best-fitting SED among the BC03 template SEDs. After comparing the extracted R_c flux with the expected flux obtained from the convolution of the WFI-R_c filter response with the best-fitting SED, we used the average difference to calibrate the extracted R_c fluxes.

We computed the depth of the optical mosaic as follows. We measured the flux inside randomly distributed $1\farcs9$ diameter apertures and we fitted a Gaussian function to the symmetrized distribution of flux values. The 3σ flux limit of the R_c image is 0.53 μJy.

In order to combine the optical and IR data, we searched the IRAC catalog for the closest counterpart to each R-detected source using a search radius of $0\farcs82$. The precise technique adopted is described in I. Baronchelli et al. (2016, in preparation). We found an optical counterpart for ~55% of

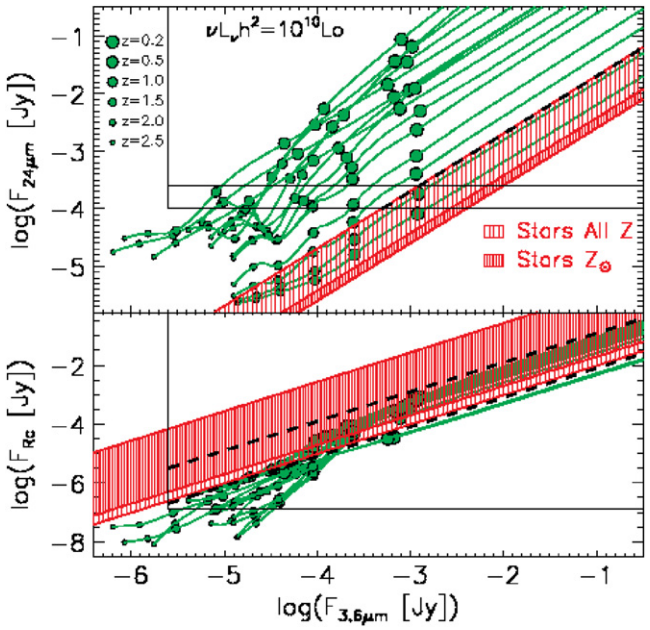

Figure 9. IRAC 3.6, MIPS 24 μm, and R_c fluxes for a library of templates including both stars (red, using the stellar models of Kurucz 1993) and galaxies (green, in the range $0 < z < 2.5$ and normalized to $\nu L_\nu h^2 = 10^{10} L_\odot$ at 3.6 μm). The selection thresholds used are represented with dashed black lines. The black boxes represent the areas covered by the plots of Figure 10.

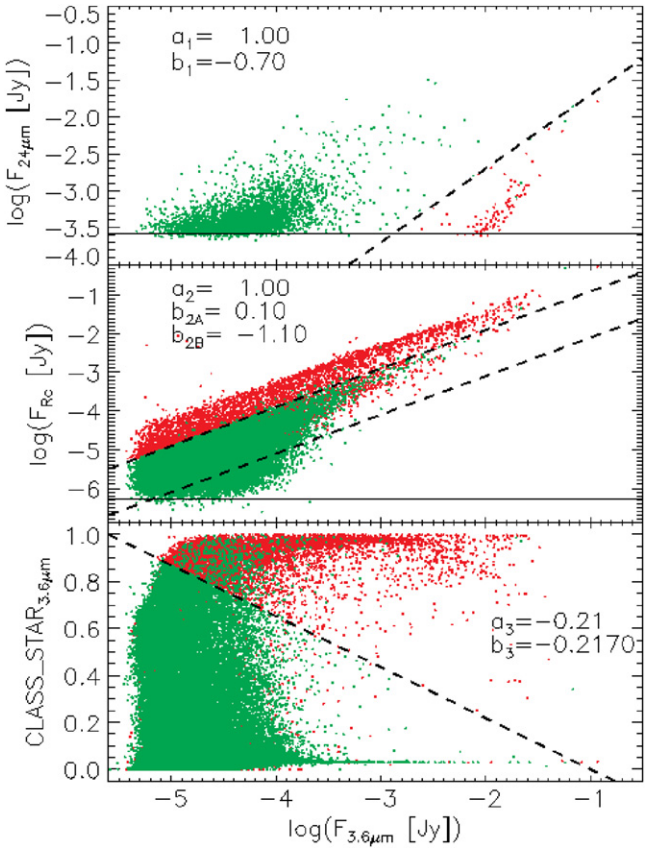

Figure 10. Galaxy/star separation. Same as Figure 9, but plotting the measurement for the objects detected in the SIMES field. In each panel, green points show sources that have been classified as galaxies by one of our criteria (see the text for details).

the IRAC-detected sources in our catalog which are covered in the R_c band.

3.4. Galaxy/Star Separation

We perform the galaxy/star separation only in the central square degree area covered by the optical data. Our separation criteria, described in detail below, are based on a combination of diagnostics using optical, 3.6 and 24 μm fluxes, as well as the surface brightness profile of each source from the optical data. Our selection criteria were calibrated using the stellar spectral models of Kurucz (1993) and a representative set of galaxy SED templates from Polletta et al. (2007), including ellipticals, spiral galaxies, starburst galaxies, and QSO templates.

We considered galaxy models in the range $0 < z < 2.5$ and with $\nu L_\nu h^2 = 10^{10} L_\odot$ at 3.6 μm, close to the characteristic L^* luminosity (e.g., Babbedge et al. 2006; Franceschini et al. 2006). We used the Kurucz (1993) stellar models with abundances relative to solar ranging from $\log(Z) = 1.0$ to $\log(Z) = -5.0$. In Figure 9, the differences between the areas occupied by the solar metallicity models and by the models with all the possible metallicities are shown. For each modeled star or galaxy, we computed the expected fluxes in the 3.6 μm, 24 μm, and R_c bands. In Figure 9, galaxy tracks are shown in green (different sizes correspond to different redshifts). Regions in the diagnostic diagrams occupied by stars are shown as the shaded red band.

The bulk of the stellar emission for a galaxy is located at $\lambda \sim 1.6$ μm (Simpson & Eisenhardt 1999; Sawicki 2002). Stars are generally fainter at longer wavelengths, especially at the SPIRE wavelengths, where the galaxy spectra is dominated by the dust thermal emission. For this reason, among the SPIRE sources, the probability of detecting a star is negligible if compared to that of detecting a galaxy. Therefore, we classify as a galaxy any object detected in one of the SPIRE bands. This assumption is confirmed by a visual inspection of the SPIRE sources on the IRAC images where the bright 3.6 μm saturated stars are not SPIRE detected.

Then, following our diagnostics, we identify stars in the 3.6 μm versus MIPS 24 plane (top panels of Figures 9 and 10). All sources with $\log(F_{24}\,[\mathrm{Jy}]) < \log(F_{3.6\,\mu\mathrm{m}}) - 0.7$ are classified as stars. Because of the bright MIPS 24 flux limit ($\log F_{24}\,[\mathrm{Jy}] \sim -3.6$), this selection misses faint IRAC-detected stars. We thus implement two additional constraints, based on the $R_c - 3.6$ μm color (bottom panel of Figure 9 and middle panel of Figures 10) and the SExtractor CLASS_STAR[26] parameter measured in the 3.6 μm image (bottom panel in Figure 10). The SPIRE and 24 μm undetected sources are classified as stars when $\log(F_{R_c}\,[\mathrm{Jy}]) > \log(F_{3.6\,\mu\mathrm{m}}) + 0.1$, and as galaxies when $\log(F_{R_c}\,[\mathrm{Jy}]) < \log(F_{3.6\,\mu\mathrm{m}}) - 1.1$. Between these two limits, or when no SPIRE, MIPS, or R_c counterparts are found, we rely on the combination of the 3.6 μm flux and the CLASS_STAR parameter to identify stars in our sample.

The reliability of the SExtractor CLASS_STAR parameter worsens at the faintest and brightest IRAC fluxes. At low fluxes (i.e., $F_{3.6\,\mu\mathrm{m}} \lesssim 10^{-4}$ Jy), the shape of a galaxy looks similar to that of a point-like source, while the PSF wings of the brightest objects (i.e., $F_{3.6\,\mu\mathrm{m}} \gtrsim 10^{-2.0}$ Jy) can be incorrectly interpreted as due to an extended

[26] CLASS_STAR = 0 for galaxies, = 1 for stars. This SExtractor output parameter quantifies the similarities between a source surface brightness profile and the profile of a point-like source.

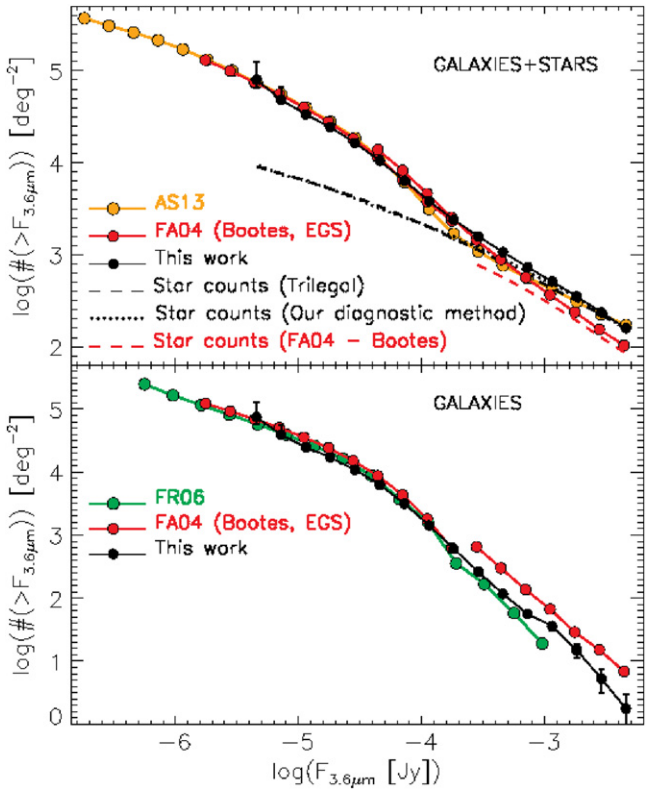

Figure 11. Top panel: *Total* (galaxy+stars) completeness-corrected integral number counts at 3.6 μm from the SIMES survey (black symbols and line). Literature results are also shown in the figure as indicated by the legend, with AS13 = Ashby et al. (2013), FA04 = Fazio et al. (2004a), and FR06 = Franceschini et al. (2006). The observed and simulated (using *TRILEGAL* code) star counts computed in the SIMES field are represented by dotted and dashed black lines. FA04 star counts in the Boötes field are represented by a dashed red line. The FA04 counts are reported here for both the EGS (faint end) and the Boötes (bright end) field. For the Boötes field, source counts are provided fainter than stars and galaxies could be reliably separated using the method described in FA04. Above $F_{3.6\,\mu m} \sim 10^{-3.7}$ Jy, the *total* counts of AS13 are fully reproduced by stars alone.

profile by SExtractor. For these reasons, we introduce a flux dependent CLASS_STAR threshold: a source is identified as a star if CLASS_STAR $> -0.21\log(F_{3.6\,\mu m}[\mathrm{Jy}]) - 0.217$. We visually checked the correct identifications of all bright sources ($F_{3.6\,\mu m} > 10^{-3.2}$ Jy) using the R_c image, correcting our counts for saturated stars wrongly identified as galaxies.

In order to assess the reliability of our diagnostic method, we compared our stellar number counts with those expected from a Milky Way model of stellar distribution. To compute the simulated stellar number counts, we used the population synthesis code *TRILEGAL*[27] (Girardi et al. 2005) considering the position of the SIMES field. The result of this comparison is visible in Figure 11 where the simulated stellar number counts are represented by a dashed line while the counts of stars identified through our diagnostic method are reported using a dotted line. At all fluxes, we observe good agreement between observed and simulated stellar counts, confirming the reliability of our method.

[27] More information on this code can be found at: http://stev.oapd.inaf.it/cgi-bin/trilegal.

4. RESULTS

The IRAC-based multiwavelength photometric catalog together with the IRAC 3.6 and 4.5 μm mosaics are released through the NASA/IPAC Infrared Science Archive (IRSA). In the following sections, we use this catalog to measure galaxy integral number counts (Section 4.1) and to search for $z \gtrsim 1.3$ galaxy clusters (Section 4.2). These are preliminary results, illustrative of those that will be allowed by the survey. We anticipate that future papers will improve the analysis once the deep optical Dark Energy Survey (Flaugher 2005) and CTIO-r (L. Barrufet et al. 2016, in preparation) data become available over the full survey area.

4.1. Cumulative Number Counts

We derive the galaxy-only and galaxy+stars (*total*) number counts from the 3.6 μm map, and compare them with the results of Franceschini et al. (2006, FA04), Ashby et al. (2013, FR06), and Ashby et al. (2013, AS13). We computed the *total* counts in the entire SIMES field and the *galaxies*-only counts in the central square degree, where we use the optical R_c band for the galaxy/star separation. All the number counts are corrected for incompleteness, with the values presented in Table 1. We report the completeness-corrected SIMES 3.6 μm integral number counts (both for galaxies+stars, and galaxies only), with the associated uncertainties, in Table 4.

The comparison between the cumulative SIMES number counts below $10^{-2.35}$ Jy and those presented in Fazio et al. (2004a), Franceschini et al. (2006), and Ashby et al. (2013) are shown in Figure 11. Out of the three fields presented in FA04, we only compare their low- and intermediate-depth fields (more similar to the data presented here), i.e., $\sim 3 \times 3$ area in the the Boötes field and $0.^{\circ}17 \times 2.^{\circ}0$ area in the EGS field, respectively. The FA04 *galaxy* and *total* number counts in the EGS field are presented in differential form, starting at the highest flux of $10^{-3.76}$ Jy. To convert them from differential to cumulative, we use our cumulative *galaxy* number counts at $10^{-3.76}$ Jy as a starting point. For the FA04 counts in the Boötes field, we do not use any starting point because they are reported through high fluxes (i.e., $10^{-1.76}$ Jy) where counts assume fractional values. FR06 presents cumulative number counts for galaxy only and no starting point is needed. On the other hand, AS13 presents *total* differential counts. As for the FA04 EGS counts, we used the SIMES cumulative counts at the flux of the brightest AS13 bin as staring point.

At 3.6 μm fluxes fainter than $\sim 10^{-4}$ Jy, our cumulative *galaxy* number counts, shown in the bottom panel of Figure 11, agree well with the three reference surveys. Above $\sim 10^{-4}$ Jy, differences are observed among all the works. Our galaxy counts fall in between those of FA04 for the Boötes field and the FR06 counts. The scatter at bright fluxes is likely ascribable to two main reasons. First, the field to field variation combined with the bias against bright sources affecting deep field small areas. The deep GOODS-south area (Dickinson et al. 2003) analyzed in FR06, among other reasons, was selected for being far from bright sources. A second likely explanation is the uncertainty in the galaxy/star separation. In particular, we note that the difference between our galaxy counts in the brightest bin and the FA04 counts at the same flux level can be fully explained with a <5% uncertainty in our corresponding stellar counts.

Table 4
Raw and Completeness Corrected Integral Number Counts at 3.6 μm

Flux	Raw Counts ($>S_{3.6}$)		Corr.	Corrected Counts ($>S_{3.6}$)					
(log(Jy))	N_{GAL} (deg^{-2})	N_{TOT} (deg^{-2})	Fact.	N_{GAL} (deg^{-2})	N^{Inf}_{GAL} (deg^{-2})	N^{Sup}_{GAL} (deg^{-2})	N_{TOT} (deg^{-2})	N^{Inf}_{TOT} (deg^{-2})	N^{Sup}_{TOT} (deg^{-2})
−2.34	2 ± 1	159 ± 13	1.0	2	1	3	159	154	163
−2.54	5 ± 2	236 ± 15	1.0	5	3	7	236	230	241
−2.74	15 ± 4	352 ± 19	1.0	15	11	19	352	346	359
−2.94	36 ± 6	511 ± 23	1.0	36	30	42	511	503	519
−3.14	56 ± 8	735 ± 27	1.0	56	49	63	735	725	745
−3.34	117 ± 11	1069 ± 33	1.0	117	107	127	1069	1057	1081
−3.54	263 ± 16	1583 ± 40	1.0	263	247	278	1583	1568	1597
−3.74	604 ± 25	2388 ± 49	0.997	603	580	627	2395	2377	2414
−3.94	1416 ± 38	3803 ± 62	0.990	1421	1385	1457	3841	3817	3865
−4.14	3116 ± 56	6250 ± 79	0.981	3150	3096	3204	6373	6341	6405
−4.34	6151 ± 78	10187 ± 101	0.972	6262	6188	6338	10481	10443	10522
−4.54	10646 ± 103	15832 ± 126	0.963	10904	10802	11010	16434	16376	16503
−4.74	16629 ± 129	23149 ± 152	0.954	17143	17012	17292	24274	24194	24391
−4.94	23892 ± 155	31579 ± 178	0.941	24859	24679	25968	33543	33407	34820
−5.14	32069 ± 179	39748 ± 199	0.827	38908	34570	56867	48091	43760	66032
−5.34	36886 ± 192	43923 ± 210	0.549	74959	57300	126954	79997	64693	125058

Note.
[a] For the raw counts, the uncertainty is the Poissonian error, while for the completeness-corrected counts, we also consider the asymmetrical uncertainty on the estimated completeness curve.

The star counts in the SIMES area agree well with the counts simulated using the *TRILEGAL* software (Girardi et al. 2005). For the *TRILEGAL* simulation, based on a statistical description of the stellar distribution in the Milky Way, we set the same coordinates of the SIMES field in order to obtain comparable results. Instead, the FA04 stellar counts refer to a different area of the sky (Boötes), where stellar counts are expected to be lower, because of the higher galactic latitude. This is indeed observed in FA04 (upper panel of Figure 11) and it is confirmed by the results of a second *TRILEGAL* simulation that we performed in an area centered in the (Boötes) region. In the brightest flux bin, simulated stellar counts resulted ∼20% lower than FA04 real counts. This indicates that the different galaxy counts in the SIMES and Boötes fields are unlikely due to an underestimation of FA04 stellar counts. Similar differences in stellar counts, when comparing different areas of the sky, can be observed e.g., in Papovich C. et al. (2015).

4.2. Selection of Clusters at Intermediate Redshifts

Galaxy clusters—through their space density and evolution with cosmic time—provide crucial information on the physical processes involved in cosmic structure formation. Representing the most extreme density environments, they provide galaxy samples with near coeval formation histories, and are thus ideal laboratories in which to investigate the interplay between galaxy evolution and environment, including the relative importance of triggering/quenching of SF and AGN activity on galaxy assembly. Papovich et al. (2010) extended the search for galaxy clusters to $z > 1.5$ by selecting galaxy cluster candidates from the SWIRE survey solely as over-densities of galaxies with red IRAC colors, satisfying $[3.6]-[4.5] > -0.2$ mag (see also Rettura et al. 2014, for a recent application of this technique). The idea behind the method is simple, and is based on the 1.6 μm stellar peak progressively moving out of the 3.6 μm and entering the 4.5 μm filter as redshift increases above $z \sim 0.7$.

In order to identify over-densities of red galaxies, we proceeded in a manner similar to Rettura et al. (2014). Briefly, before searching for spatial over-densities, we preselected only those galaxies which satisfied the following conditions: IRAC $[3.6]-[4.5] > -0.2$, $19.5 < [4.5] < 21.5$, and S/N > 3 and 5, at 3.6 and 4.5 μm, respectively. Similar cuts have been effectively used by various programs (Galametz et al. 2010, 2013; Papovich et al. 2010; Gettings et al. 2012; Muzzin et al. 2013; Rettura et al. 2014). In the central square degree where our WFI-R_c data are available, we also require selected galaxies to have $F_{R_c} < 14.5$ μJy (this condition helps to broadly reject contaminants at $z < 0.3$). For each galaxy j in the selected sample, we then computed the quantity $\Delta N_{CC} = N_{1'} - N_{5'-8'}$, i.e., the difference between the number of red galaxies within 1.′0 from the jth galaxy (N_1) and the number of red galaxies in the background, which we computed inside an annulus of radius 5.′0–8.′0, normalized to a circular area of 1.′0 radius ($N_{5'-8'}$). All of the counts are corrected for incompleteness using the results of the simulation discussed in Section 2.3, and computing the number of galaxies within a given distance from galaxy j, as $N_j = \sum_i^N \frac{1}{C_i(3.6)}$, where the sum is over all N galaxies within 1.′0 from galaxy j, and C_i is the completeness corresponding to the 3.6 μm flux of galaxy i.

The observed distribution of the excess number of objects (within 1.′0) with respect to the local background (ΔN_{CC}) is shown in Figure 12 (top panel), together with the best-fit Gaussian distribution computed using values of $\Delta N_{CC} < 3$. The best-fit Gaussian distribution has a mean of 0.45 and a standard deviation of $\sigma = 4.6$, consistent with the best-fit values obtained by Rettura et al. (2014) on similar depth data, on more than ten times the area. The Gaussian function can be used to describe the probability of observing a given excess number of objects around a galaxy, under the null hypothesis (H) that the galaxy does not belong to a cluster. In order to identify only those galaxies located within clusters we proceed following the Benjamini–Hochberg procedure (BH; Benjamini & Hochberg 1995), which minimizes the false discovery rate at

Table 5
Multiwavelength Catalog Columns and Description[a]

Column	Example	Content
ID	163210	Identification number for IRAC 1 detected sources.
R.A._I1	71.040682	IRAC 3.6 μm R.A. coordinate
decl._I1	−53.615640	IRAC 3.6 μm decl. coordinate
FLUX_I1	4.58311	IRAC 3.6 μm total mJy flux (FLUX_AUTO)
FLUXERR_I1	0.00820884	IRAC 3.6 μm mJy flux associated uncertainty
N_SIGMA	813.635	IRAC 3.6 μm Signal to noise ratio connected to average coverage
FLUX_I2	3.05153	IRAC 4.5 μm total mJy flux (FLUX_AUTO, I1 prior position used)
FLUXERR_I2	0.00781307	IRAC 4.5 μm mJy flux associated uncertainty
R.A._24	71.040554	R.A. coordinate for MIPS 24 μm sources corrected for systematic shift ($-0\farcs165$)
decl._24	−53.615536	decl. coordinate for MIPS 24 μm sources corrected for systematic shift ($-0\farcs489$)
O_R.A._24	71.040600	original RA coordinate for MIPS 24 sources[b]
O_decl._24	−53.615400	original decl. coordinate for MIPS 24 sources[b]
FLUX_24	3.98400	MIPS 24 μm mJy flux[b]
FLUXERR_24	0.0600000	MIPS 24 μm mJy flux uncertainty[b]
FLUX_70	20.0000	MIPS 70 μm mJy flux[b]
FLUXERR_70	3.63636	MIPS 70 μm mJy flux uncertainty[b]
R.A._SPIRE	71.039836	R.A. coordinate for SPIRE sources corrected for systematic shift ($-0\farcs199$)
decl._SPIRE	−53.615458	decl. coordinate for SPIRE sources corrected for systematic shift ($-0\farcs443$)
O_R.A._SPIRE	71.039856	original R.A. SPIRE coordinate[c]
O_decl._SPIRE	−53.615330	original decl. SPIRE coordinate[c]
FLUX_250	92.635274	SPIRE 250 μm mJy flux[c]
FLUXERR_250	2.3467732	SPIRE 250 mJy flux uncertainty[c]
FLUX_350	38.933088	SPIRE 350 μm mJy flux[c]
FLUXERR_350	4.4716398	SPIRE 350 mJy flux uncertainty[c]
FLUX_500	20.702205	SPIRE 500 μm flux[c]
FLUXERR_500	4.0425355	SPIRE 500 mJy flux uncertainty[c]
R.A._OPT	−53.615583	R.A. coordinate for WFI-R_c
decl._OPT	−53.615583	decl. coordinate for WFI-R_c
FLUX_R_WFI	3.87101	WFI-R_c total mJy flux (FLUX_AUTO)
FLUXERR_R_WFI	0.00968389	WFI-R_c total mJy flux uncertainty
P1	0.84638566	SPIRE–MIPS reliability indicator (ranges from 0 to 1, where 0 = bad, 1 = good)
N_MIPS_SPIRE	1	Number of MIPS counterparts for the SPIRE source
P2	0.85814963	MIPS–IRAC reliability indicator (ranges from 0 to 1, where 0 = bad, 1 = good)
N_IRAC_MIPS	1	Number of IRAC counterparts for the MIPS source
P3	0.80220842	SPIRE–IRAC reliability indicator (ranges from 0 to 1, where 0 = bad, 1 = good)
N_IRAC_SPIRE	1	Number of IRAC counterparts for the SPIRE source
CLASS_STAR_I1	0.0286267	SExtractor CLASS_STAR parameter for IRAC 3.6 μm (ranges from 0 to 1, where 0 = galaxy, 1 = star)
A_I1	6.28684	Semimajor axis in arcseconds
B_I1	3.39138	Semiminor axis in arcseconds
SIGMA	0.00145476	IRAC 3.6 μm sky sigma value (depends on the coverage)
COVERAGE	9.66118	Average coverage computed over an area of 49 pixels centered on the 3.6 μm coordinates
AP1_FLUX_I1	0.00118364	IRAC 3.6 μm mJy aperture flux ($4\farcs8$ ap. diameter).
AP1_FLUXERR_I1	0.00118364	IRAC 3.6 μm mJy aperture flux uncertainty ($4\farcs8$ ap. diameter).
AP2_FLUX_I1	0.00184539	IRAC 3.6 μm mJy aperture flux ($7\farcs2$ ap. diameter).
AP2_FLUXERR_I1	0.00184539	IRAC 3.6 μm mJy aperture flux uncertainty ($7\farcs2$ ap. diameter).
AP3_FLUX_I1	0.00291065	IRAC 3.6 μm mJy aperture flux ($12\farcs0$ ap. diameter).
AP3_FLUXERR_I1	0.00291065	IRAC 3.6 μm mJy aperture flux uncertainty ($12\farcs0$ ap. diameter).
AP1_FLUX_I2	0.00118364	IRAC 4.5 μm mJy aperture flux ($4\farcs8$ ap. diameter).
AP1_FLUXERR_I2	0.00118364	IRAC 4.5 μm mJy aperture flux uncertainty ($4\farcs8$ ap. diameter).
AP2_FLUX_I2	0.00184539	IRAC 4.5 μm mJy aperture flux ($7\farcs2$ ap. diameter).
AP2_FLUXERR_I2	0.00184539	IRAC 4.5 μm mJy aperture flux uncertainty ($7\farcs2$ ap. diameter).
AP3_FLUX_I2	0.00291065	IRAC 4.5 μm mJy aperture flux ($12\farcs0$ ap. diameter).
AP3_FLUXERR_I2	0.00291065	IRAC 4.5 μm mJy aperture flux uncertainty ($12\farcs0$ ap. diameter).

Notes.
[a] All the fluxes are expressed in mJy and the coordinates are in degrees. All the fluxes are "*total*" and do not need any further aperture correction, unless differently specified. The IRAC aperture fluxes reported here for the $4\farcs8$, $7\farcs2$, and $12\farcs0$ diameter apertures are not aperture corrected; to obtain the correspondent *total* flux, the IRAC handbook aperture corrections are needed. The counterpart distances are expressed in arcseconds. The catalog is released through the NASA/IPAC Infrared Science Archive (IRSA) service.
[b] From Clements et al. (2011).
[c] From SPIRE XID catalogs (DR2, Roseboom et al. 2010; Smith et al. 2012; Wang et al. 2014).

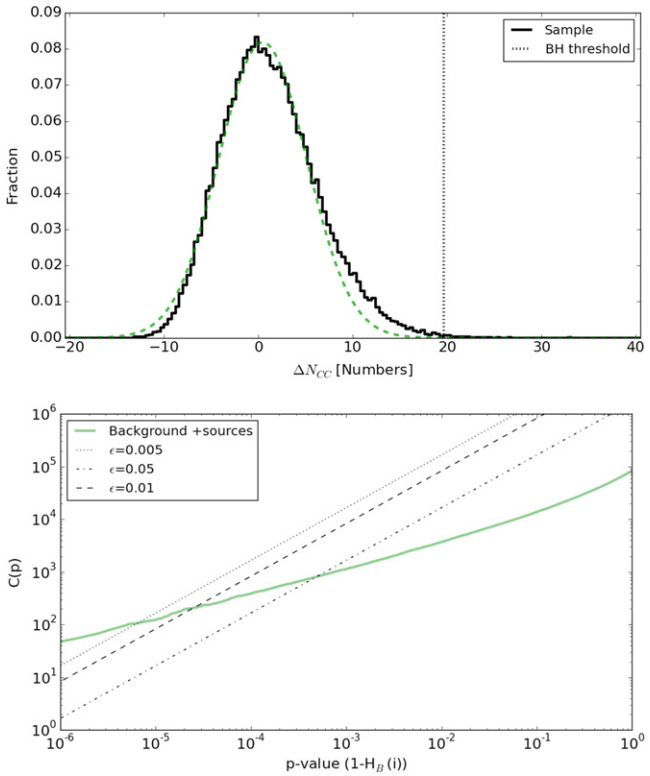

Figure 12. Top panel: distribution of the excess number of objects (within 1.′0) with respect to the local background for all galaxy candidates at $z > 1.3$. The green dashed line shows the best-fit Gaussian distribution fitted for values of $\Delta N_{CC} < 7$, and the probability of observing a given excess number of objects around a galaxy, under the null hypothesis that the galaxy does not belong to a cluster. Bottom panel: illustration of the Benjamini–Hochberg procedure: the green solid line shows the cumulative distribution of galaxies' p-values computed under the assumption of the null hypothesis (i.e., using the Gaussian best-fit parameters). The black lines correspond to different levels of contamination of the final sample.

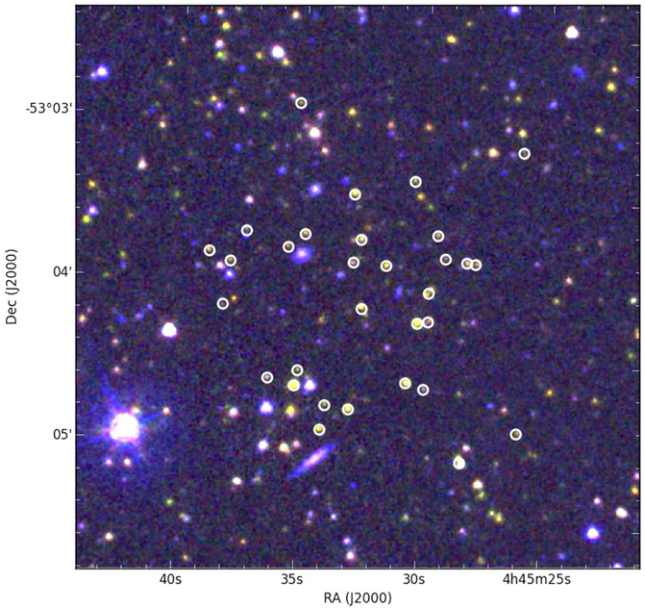

Figure 13. False color image (red = 4.5 μm, green = 3.6 μm, and blue = R_c) showing a 3.′7 × 3.′7 region around one of the galaxy cluster identified in the central square degree where optical data are available. Open circles show galaxies with red 3.6−4.5 μm color, 3.6 μm and R_c magnitudes fainter than 18.7 and 21, respectively.

a level ϵ. Briefly, for each galaxy we compute its p-value under the null hypothesis H. The p-values are ordered in increasing order and denoted by p_1 ,...,p_N. The cumulative distribution of the p-values is shown in Figure 12, bottom panel. Note that the value of $C(p)$ corresponds to the index j of each galaxy (the galaxies were sorted according to their p-value). For a given ϵ, we compute the critical p-value by finding the largest j such that $p_j \leqslant \frac{k}{N}\epsilon$. The corresponding ΔN_{CC} is then the cutoff value we use to identify galaxies belonging to a cluster. The BH procedure ensures that the false discovery rate is smaller than ($\epsilon \times 100$)%. In Figure 12 we show the curves corresponding to various values of ϵ. For the cluster selection we used the conservative value $\epsilon = 0.005$, which corresponds to objects with $\Delta N_{CC} \geqslant 19.7$ (indicated by the vertical dotted line in the top panel of Figure 12).

The procedure above identifies galaxies residing in over dense regions, and thus can identify multiple galaxies belonging to the same over density. We follow Papovich (2008) and Rettura et al. (2014) and merge the cluster candidates by applying a friends-of-friends algorithm with a linking length of 1.′5, corresponding to approximately 0.8 Mpc at $z = 1.5$. With this algorithm, we identify 27 unique galaxy clusters. An example of a detected cluster in the central region where optical data are available is shown in Figure 13. The density of clusters in the SIMES area (3.8 ± 0.7 clusters deg^{-2}) is consistent with the density found by Rettura et al. (2014; 3.0 ± 0.2 clusters deg^{-2}).

5. SUMMARY

We presented SIMES in the SEP field and the multi-wavelength catalog of sources based on the 3.6 μm detections. The survey covers an area of 7.74 deg^2 to a depth of ∼5.80 μJy (3σ) at 3.6 μm and 5.25 μJy at 4.5 μm. We estimate 90% and 50% completeness levels in the 3.6 μm band at 14 and 9 μJy, respectively. Table 5 describes all the columns in our photometric catalog.

The SIMES region has been targeted by numerous multi-wavelengths surveys spanning the UV to the far-IR and radio regimes. The addition of the *Spitzer*-IRAC observations is crucial for computing reliable photometric redshifts and stellar masses for all galaxies detected in this region by the *Herschel* satellite. The IRAC observation presented here allowed us to identify the optical/IR counterparts of the starforming galaxies and AGNs detected at the far-IR wavelengths. We included in our multiwavelength catalog the WFI-R_c, MIPS 24 μm, SPIRE 250, 350, and 500 μm fluxes of the counterparts that we identified by searching for the closest neighbor. The reliability (i.e., fraction of spurious detections introduced) of these associations is quantified through the indicator "P" that we computed for each MIPS and SPIRE detected source. The possibility of a direct IRAC–SPIRE association is also discussed. The full catalog is available through the NASA/IPAC IRSA.

We reported 3.6 μm galaxy and *total* (galaxy and stars) number counts in the SIMES field and compared them with literature results obtained in different fields. Below $F_{3.6\mu m} = 10^{-4.0}$ Jy our galaxy counts are more in agreement with Franceschini et al. (2006) than with Fazio et al. (2004a). Above $F_{3.6\mu m} = 10^{-4.0}$ Jy galaxy counts in the SIMES field are in between those of Fazio et al. (2004a) and Franceschini et al. (2006). While our *galaxy* number counts are computed within

the area with optical imaging, our *total* counts are calculated in the whole SIMES area.

Finally, using the method proposed in Papovich et al. (2010), we identified 27 galaxy clusters at $z > 1.3$. Although preliminary (only part of the field at this point is covered by optical data), the surface density of the galaxy clusters in SIMES is consistent with that reported in Rettura et al. (2014).

Further deep observations in optical bands will soon be available (I. Baronchelli et al. 2016, in preparation). Such observations will allow us to improve our estimates and the measure of precise photometric redshifts for the galaxies in the SIMES field. The correlation among the near- and far-IR bands will be further improved using the available 90 μm *Akari* data presented in Małek et al. (2014). These data will also allow for an extensive study of the dust thermal emission in these spectral regions.

We thank the referee for the useful comments that improved the presentation of the paper. I.B. and G.R. acknowledge support from ASI (Herschel Science Contract 2011aI/005/011/0). C.S. and I.B. acknowledge support from NASA JPL/Spitzer grant RSA 1449911, provided for the SIMES project. S.M. acknowledges financial support from the Institut Universitaire de France (IUF), of which she is senior member. M.V. acknowledges support from the European Commission Research Executive Agency (FP7-SPACE-2013-1 GA 607254) and the Italian Ministry for Foreign Affairs and International Cooperation (PGR GA ZA14GR02). This research has made use of data from the HerMES project (http://hermes.sussex.ac.uk/). HerMES is a Herschel Key Program using Guaranteed Time from the SPIRE instrument team, ESAC scientists, and a mission scientist. The HerMES data were accessed through the Herschel Database in Marseille (HeDaM—http://hedam.lam.fr), operated by CeSAM and hosted by the Laboratoire d'Astrophysique de Marseille. This research has made use of the NASA/IPAC Infrared Science Archive, which is operated by the Jet Propulsion Laboratory, California Institute of Technology, under contract with the National Aeronautics and Space Administration. M.V. acknowledges support from the European Commission Research Executive Agency (FP7-SPACE-2013-1 GA 607254) and the Italian Ministry for Foreign Affairs and International Cooperation (PGR GA ZA14GR02).

REFERENCES

Ashby, M. L. N., Willner, S. P., Fazio, G. G., et al. 2013, ApJ, 769, 80
Babbedge, T. S. R., Rowan-Robinson, M., Vaccari, M., et al. 2006, MNRAS, 370, 1159
Bedregal, A. G., Scarlata, C., Henry, A. L., et al. 2013, ApJ, 778, 126
Benjamini, Y., & Hochberg, Y. 1995, Journal of the Royal Statistical Society Series B, 57, 289
Bertin, E., & Arnouts, S. 1996, A&AS, 117, 393
Bolzonella, M., Miralles, J., & Pelló, R. 2000, A&A, 363, 476
Bruzual, G., & Charlot, S. 2003, MNRAS, 344, 1000
Capak, P. L., Teplitz, H. I., Brooke, T. Y., Laher, R., & Science Center, S. 2013, in American Astronomical Society Meeting Abstracts, #221, 340.06
Chary, R., & Elbaz, D. 2001, ApJ, 556, 562
Clements, D. L., Bendo, G., Pearson, C., et al. 2011, MNRAS, 411, 373
Daddi, E., Dickinson, M., Morrison, G., et al. 2007, ApJ, 670, 156
Dale, D. A., Gil de Paz, A., Gordon, K. D., et al. 2007, ApJ, 655, 863
Dickinson, M., Giavalisco, M., & GOODS Team 2003, The Mass of Galaxies at Low and High Redshift, ed. R. Bender, & A. Renzini (Berlin: Springer-Verlag), 324
Elbaz, D., Dickinson, M., Hwang, H. S., et al. 2011, A&A, 533, A119
Fazio, G. G., Ashby, M. L. N., Barmby, P., et al. 2004a, ApJS, 154, 39
Fazio, G. G., Hora, J. L., Allen, L. E., et al. 2004b, ApJS, 154, 10
Flaugher, B. 2005, IJMPA, 20, 3121
Franceschini, A., Rodighiero, G., Cassata, P., et al. 2006, A&A, 453, 397
Galametz, A., Stern, D., Pentericci, L., et al. 2013, A&A, 559, A2
Galametz, A., Vernet, J., De Breuck, C., et al. 2010, A&A, 522, A58
Gettings, D. P., Gonzalez, A. H., Stanford, S. A., et al. 2012, ApJL, 759, L23
Girardi, L., Groenewegen, M. A. T., Hatziminaoglou, E., & da Costa, L. 2005, A&A, 436, 895
Graham, A. W., & Driver, S. P. 2005, PASP, 22, 118
Griffin, M. J., Abergel, A., Abreu, A., et al. 2010, A&A, 518, L3
Gruppioni, C., Pozzi, F., Rodighiero, G., et al. 2013, MNRAS, 432, 23
Kirkpatrick, A., Pope, A., Alexander, D. M., et al. 2012, ApJ, 759, 139
Kron, R. G. 1980, ApJS, 43, 305
Kurucz, R. 1993, ATLAS9 Stellar Atmosphere Programs and 2 km/s grid. Kurucz CD-ROM No. 13 (Cambridge, MA: Smithsonian Astrophysical Observatory)
Magnelli, B., Lutz, D., Santini, P., et al. 2012, A&A, 539, A155
Makovoz, D., & Khan, I. 2005, in ASP Conf. Ser. 347, Astronomical Data Analysis Software and Systems XIV, ed. P. Shopbell, M. Britton, & R. Ebert (San Francisco, CA: ASP), 81
Makovoz, D., Khan, I., & Moshir, M. 2005, PASP, 117, 274
Małek, K., Pollo, A., Takeuchi, T. T., et al. 2014, A&A, 562, A15
Matsuhara, H., Wada, T., Matsuura, S., et al. 2006, PASJ, 58, 673
Matsuura, S., Shirahata, M., Kawada, M., et al. 2011, ApJ, 737, 2
Muzzin, A., Wilson, G., Demarco, R., et al. 2013, ApJ, 767, 39
Noeske, K. G., Faber, S. M., Weiner, B. J., et al. 2007, ApJL, 660, L47
Oliver, S. J., Bock, J., Altieri, B., et al. 2012, MNRAS, 424, 1614
Papovich, C. 2008, ApJ, 676, 206
Papovich, C., Momcheva, I., Willmer, C. N. A., et al. 2010, ApJ, 716, 1503
Papovich, C., Shipley, H. V., Mehrtens, N., et al. 2015, ApJS, submitted
Peng, Y.-j., Lilly, S. J., Kovač, K., et al. 2010, ApJ, 721, 193
Pilbratt, G. L., Riedinger, J. R., Passvogel, T., et al. 2010, A&A, 518, L1
Poglitsch, A., Waelkens, C., Geis, N., et al. 2010, A&A, 518, L2
Polletta, M., Tajer, M., Maraschi, L., et al. 2007, ApJ, 663, 81
Rettura, A., Martinez-Manso, J., Stern, D., et al. 2014, ApJ, 797, 109
Rieke, G. H., Young, E. T., Engelbracht, C. W., et al. 2004, ApJS, 154, 25
Rodighiero, G., Cimatti, A., Gruppioni, C., et al. 2010, A&A, 518, L25
Rodighiero, G., Daddi, E., Baronchelli, I., et al. 2011, ApJL, 739, L40
Rosario, D. J., Santini, P., Lutz, D., et al. 2012, A&A, 545, A45
Roseboom, I. G., Oliver, S. J., Kunz, M., et al. 2010, MNRAS, 409, 48
Santini, P., Maiolino, R., Magnelli, B., et al. 2014, A&A, 562, A30
Sawicki, M. 2002, AJ, 124, 3050
Schlegel, D. J., Finkbeiner, D. P., & Davis, M. 1998, ApJ, 500, 525
Sedgwick, C., Serjeant, S., Pearson, C., et al. 2011, MNRAS, 416, 1862
Sérsic, J. L. 1963, BAAA, 6, 99
Simpson, C., & Eisenhardt, P. 1999, PASP, 111, 691
Smith, A. J., Wang, L., Oliver, S. J., et al. 2012, MNRAS, 419, 377
Surace, J. A., Shupe, D. L., Fang, F., et al. 2005, BAAS, 37, 63.01
Trenti, M., & Stiavelli, M. 2008, ApJ, 676, 767
Wang, L., Viero, M., Clarke, C., et al. 2014, MNRAS, 444, 2870
Werner, M. W., Roellig, T. L., Low, F. J., et al. 2004, ApJS, 154, 1
Wuyts, S., Förster Schreiber, N. M., van der Wel, A., et al. 2011, ApJ, 742, 96